

See discussions, stats, and author profiles for this publication at: <https://www.researchgate.net/publication/230646579>

# Enhanced thermoelectric performance of compacted Bi<sub>0.5</sub>Sb<sub>1.5</sub>Te<sub>3</sub> nanoplatelets with low thermal conductivity

Article in *Journal of Materials Research* · August 2011

DOI: 10.1557/jmr.2011.158

CITATIONS

21

READS

143

6 authors, including:



Chia-Jyi Liu

National Changhua University of Education

227 PUBLICATIONS 2,441 CITATIONS

[SEE PROFILE](#)



Alan B. Kaiser

Victoria University of Wellington

117 PUBLICATIONS 3,827 CITATIONS

[SEE PROFILE](#)

Some of the authors of this publication are also working on these related projects:



Preparation and Characterization of Thermoelectric Composites [View project](#)

# Enhanced thermoelectric performance of compacted $\text{Bi}_{0.5}\text{Sb}_{1.5}\text{Te}_3$ nanoplatelets with low thermal conductivity

Chia-Jyi Liu,<sup>a)</sup> Gao-Jhih Liu, Yen-Liang Liu, and Liang-Ru Chen

*Department of Physics, National Changhua University of Education, Changhua 500, Taiwan, Republic of China*

Alan B. Kaiser

*MacDiarmid Institute for Advanced Materials and Nanotechnology, Victoria University of Wellington, Wellington, New Zealand*

(Received 14 December 2010; accepted 4 May 2011)

We report fabrication of compacted  $\text{Bi}_{0.5}\text{Sb}_{1.5}\text{Te}_3$  nanoplatelets using hydrothermal methods followed by cold pressing and sintering in an evacuated ampoule at various temperature of 300–380 °C. The compacted  $\text{Bi}_{0.5}\text{Sb}_{1.5}\text{Te}_3$  sintered at 340 °C has the highest power factor of  $11.6 \mu\text{W}/\text{cm}\cdot\text{K}^2$  and its thermal conductivity is  $0.37 \text{ W}/\text{m}\cdot\text{K}$  at 295 K, which is very low as compared to the typical value of  $1 \text{ W}/\text{m}\cdot\text{K}$ . The resulting dimensionless figure of merit  $ZT$  is 0.93 at 295 K.

## I. INTRODUCTION

Thermoelectric materials can produce electrical power via the Seebeck effect and provide cooling capability via the Peltier effect without using coolants. Therefore, they can be considered as energy and environmentally friendly materials. The figure of merit ( $Z$ ) of thermoelectric materials is determined by three transport parameters and can be expressed as  $Z = \sigma S^2/\kappa$ , where  $\sigma$ ,  $S$ , and  $\kappa$  are the electrical conductivity, thermopower, and thermal conductivity, respectively. Bismuth alloys show the highest dimensionless figure of merit  $ZT$  (where  $T$  is the absolute temperature) around room temperature and are one of the most commercialized thermoelectric materials. The crystal lattice of  $(\text{Bi,Sb})_2(\text{Te,Se})_3$  has the symmetry of  $R\bar{3}m$ . The layers of atoms A(Bi,Sb) and B(Te,Se) are arranged in the order of  $-\text{B}^{(1)}-\text{A}-\text{B}^{(2)}-\text{A}-\text{B}^{(1)}-$  along the  $c$  axis.

Turning the currently best thermoelectric materials into nanoscale grain boundaries or nanostructure helps improve thermoelectric figure of merit by increasing the thermoelectric power (TEP) as a result of an enhanced density of states and by reducing thermal conductivity as a result of an increased phonon scattering.<sup>1,2</sup> Recently, the theoretical concept has been fulfilled by a significant enhancement of  $ZT$  value for nanostructured bulk of  $\text{Bi}_{2-x}\text{Sb}_x\text{Te}_3$ .<sup>3,4</sup>

Several groups reported bottom-up chemical synthesis of  $\text{Bi}_2\text{Te}_3$  nanocrystals at low temperatures of 140–150 °C using either organic solvent or water as reacting medium.<sup>5–10</sup> It is well known that the carrier concentration needs to be optimized for thermoelectric materials to achieve the best electronic transport properties due to its opposite trends with respect to electrical conductivity

and thermopower. There exist complex lattice defects in  $\text{Bi}_{2-x}\text{Sb}_x\text{Te}_3$ . The ionized defects could change the carrier concentration and hence the electronic transport properties.<sup>11</sup> Furthermore, lattice defects are known to be sensitive to sintering or annealing temperature<sup>12</sup> and play an important role to obtain good thermoelectric properties of  $\text{Bi}_{2-x}\text{Sb}_x\text{Te}_3$ . Although bottom-up chemical synthesis of  $\text{Bi}_{2-x}\text{Sb}_x\text{Te}_3$  nanocrystals is feasible at low temperatures, it is, therefore, desirable to optimize the thermoelectric properties by finding suitable sintering conditions while consolidating  $\text{Bi}_{2-x}\text{Sb}_x\text{Te}_3$  nanocrystals. In this study, the process parameter of sintering temperature is investigated to optimize the thermoelectric characteristics of pressed compacts of hydrothermally synthesized  $\text{Bi}_{0.5}\text{Sb}_{1.5}\text{Te}_3$  nanoplatelets. As a result, we find that the sample sintered at 340 °C has the largest power factor and its thermal conductivity is rather small having the size of  $0.37 \text{ W}/\text{m}\cdot\text{K}$  at 295 K, which is quite small as compared to the typical value of the corresponding material. The dimensionless figure of merit  $ZT$  is 0.93 at 297 K.

## II. MATERIALS AND METHODS

Nanoplatelets of  $\text{Bi}_{0.5}\text{Sb}_{1.5}\text{Te}_3$  were synthesized using a hydrothermal method. Te powders (6 mmol),  $\text{BiCl}_3$  (1 mmol),  $\text{SbCl}_3$  (3 mmol), ethylenediaminetetraacetic acid (8 mmol), and deionized water (70 ml) were quantitatively added into a polytetrafluoroethylene (PTFE) cylindrical container and well stirred at room temperature for 1 h. KOH (70 mmol) was then added to the above solution and stirred for 1 h, followed by adding  $\text{NaBH}_4$  (24 mmol) and stirring for another 0.5 h. The PTFE container containing the above solution was transferred to a pressure bomb and heated at 140 °C for 36 h in a box furnace.  $\text{NaBH}_4$  is required to inhibit the formation of  $\text{Bi}_2\text{O}_3$ . The resulting powders were washed by deionized

<sup>a)</sup>Address all correspondence to this author.

e-mail: liucj@cc.ncue.edu.tw

DOI: 10.1557/jmr.2011.158

water and then by absolute ethanol, followed by drying at 80 °C. The resulting powders were compacted into parallelepiped and then sealed in an evacuated Pyrex ampoule. The pressure of cold pressing is about  $2.1 \times 10^5 \text{ N/cm}^2$ . Sintering was carried out at various temperatures of 300–380 °C for 10 h to study the effects of sintering temperature on their thermoelectric characteristics.

Powder x-ray diffraction (XRD) patterns were obtained with an XRD-6000 diffractometer (Shimadzu, Kanagawa, Japan) equipped with  $\text{Fe K}\alpha$  radiation. The morphology of the samples was observed with a field emission scanning electron microscope (Hitachi S-4300 FE-SEM, Hitachi, Tokyo, Japan). The thickness of nanoplatelets was determined by an atomic force microscope (AFM) using alternating current (AC) mode (PicoScan 2100, Molecular Imaging, Tempe, AZ) by oscillating the cantilever assembly at or near the cantilever's resonant frequency using a piezoelectric crystal, for which a Si tip (force constant: 48 N/m and resonance frequency: 190 kHz, Nanosensors, Santa Clara, CA) is vibrated vertically while scanning above the film surface. Transmission electron microscope (TEM) images were taken using a JEOL JEM-2010 TEM (JEOL, Tokyo, Japan) equipped with OXFORD INCAx-sight energy dispersive x-ray (EDX, Oxford, Bucks, UK) spectrometer detector and INCAx-stream pulse processor. Electrical resistivity measurements were performed between 305 and 10 K in an Oxford closed cycle cooler cryostat using the standard four-probe techniques by reversing the current sources to cancel thermoelectric voltages. A Cernox sensor was used to monitor the ambient temperature of the sample. Temperature-dependent thermopower data were collected between 300 and 80 K using a steady technique. The thermally generated Seebeck voltage across the sample was measured using a Keithley 2182 nanovoltmeter (Keithley, Cleveland, OH). A type E differential thermocouple was used to measure the temperature difference between the hot and cold ends of the sample, which was measured using Keithley 2000 multimeter. The temperature difference was typically between 0.5 and 1 K. The TEP of the sample was obtained by subtracting the TEP of Cu Seebeck probes. Carrier concentration and mobility were determined by Hall measurements using the van der Pauw method under an applied field of 0.55 T (HMS-3000, ECOPIA, Gyeonggi-do, South Korea). Thermal conductivity measurement was carried out using transient plane source techniques<sup>13</sup> with very small temperature perturbations of the sample material by the Hot Disk thermal constants analyzer (Hot Disk, Gothenburg, Sweden). The transient plane source technique makes use of a thin sensor element in the shape of a double spiral. The Hot Disk sensor acts both as a heat source for generating temperature gradient in the sample and a resistance thermometer for recording the time-dependent temperature increase. The encapsulated sensor is sandwiched between two pieces of samples. During a preset time, 200

between temperature and time is established. A few parameters like the output of power to increase the temperature of the spiral, the measurement time for recording 200 point, and the size of the sensor are used to optimize the settings for the measurement. Since the vendor only provides the temperature coefficient of the resistivity (TCR) down to  $-80^\circ\text{C}$  for the sensor, we use TCR at room temperature as a constant in the whole investigated temperature range. Data below room temperature need further calibration for each sensor being used. However, the thermal conductivity obtained at 295 K is reliable. The uncertainty for the electrical resistivity, thermopower, and thermal conductivity is about  $\pm 3\%$ ,  $\pm 4\%$ , and  $\pm 4\%$ , respectively. The typical sample shape for electrical resistivity and thermopower is parallelepiped with the dimension of  $12.30 \times 2.30 \times 0.91 \text{ mm}^3$ , whereas typical sample shape for thermal conductivity is a circular disk with the dimensions of 14 mm in diameter and 40-mm thickness.

### III. RESULTS AND DISCUSSION

Figure 1 shows the XRD patterns of hydrothermally prepared  $\text{Bi}_{0.5}\text{Sb}_{1.5}\text{Te}_3$  nanoplatelets and sintered  $\text{Bi}_{0.5}\text{Sb}_{1.5}\text{Te}_3$  at different temperatures of 300–380 °C in an evacuated ampoule. Most of the reflection peaks can be indexed based on a rhombohedra lattice with the space group of  $R\bar{3}m$ . The (015) and (1010) reflections of the as-synthesized  $\text{Bi}_{0.5}\text{Sb}_{1.5}\text{Te}_3$  have a shoulder on left and right hand side, respectively. Both shoulders belong to (101) and (102) reflections of Te, respectively, indicating the presence of Te. The shoulders become more apparent as the hydrothermally prepared powders are subject to sintering. The density of our sintered pellets lies between 87 and 90% of the theoretical density of  $6.878 \text{ g/cm}^3$ . EDX analyses were carried out on randomly chosen five spots of each sample. The EDX spectra reveal that the composition is not homogeneous, in particular the Te content. For sample sintered at 380 °C, there are Te-rich and Te-poor spots with a large difference of Te content, which can be seen in Fig. 2 showing the EDX mapping of Te and one of the line scans across the sample.

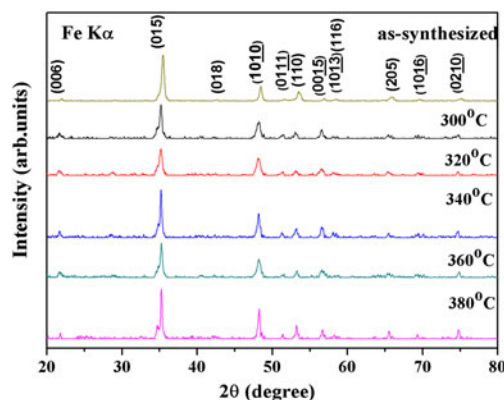


FIG. 1. Powder x-ray diffraction patterns of hydrothermally prepared  $\text{Bi}_{0.5}\text{Sb}_{1.5}\text{Te}_3$  nanoplatelets and sintered  $\text{Bi}_{0.5}\text{Sb}_{1.5}\text{Te}_3$  at various temperatures of 300–380 °C in an evacuated ampoule.

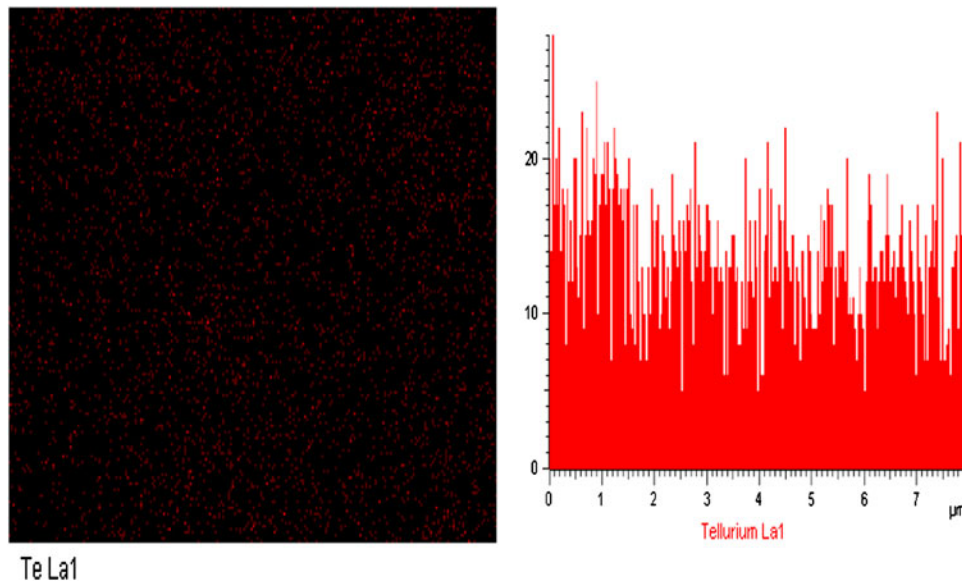


FIG. 2. The energy dispersive x-ray spectrometer mapping of tellurium and one of the line scans across the sample sintered at 380 °C.

Figure 3(a) shows the scanning electron microscope (SEM) image of hydrothermally synthesized Bi<sub>0.5</sub>Sb<sub>1.5</sub>Te<sub>3</sub> nanoplatelets having various sizes. The AFM image shown in Fig. 3(b) indicates that the nanoplatelets have a thickness of about 30–50 nm. The EDX spectra reveal that the composition of the nanoplatelets is Bi<sub>0.47</sub>Sb<sub>1.53</sub>Te<sub>2.75</sub>. The sum of atomic ratio of Bi and Sb is taken as 2 in the composition calculation.

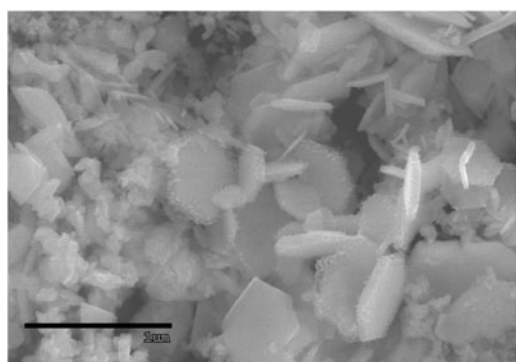
Figure 4 shows the temperature dependence of the electrical resistivity for Bi<sub>0.5</sub>Sb<sub>1.5</sub>Te<sub>3</sub> samples sintered at different temperatures of 300–380 °C. All samples display metal-like temperature dependence between 300 and 10 K except for a change from metallic to nonmetallic temperature dependence at 235 K for the sample sintered at 380 °C. Moreover, the resistivity of all samples is lower than the one which is compacted without sintering. The resistivity of the non-sintered sample is ~40 mΩ·cm at room temperature and increase with decreasing temperature. As shown in Fig. 4, it can be readily seen that the resistivity increases with increasing sintering temperature, and that there is a big jump of the resistivity as the sintering temperature is increased to 380 °C. Figure 5 shows the temperature dependence of the thermopower for Bi<sub>0.5</sub>Sb<sub>1.5</sub>Te<sub>3</sub> samples sintered at different temperatures. Samples sintered at 300–340 °C show a slope in the temperature dependence of thermopower, which resembles the slope in the temperature dependence of electrical resistivity, whereas the 380 °C-sintered sample shows a flattening and downturn in thermopower above 200 K corresponding to the change in sign of the resistivity temperature dependence. For a single and nondegenerate band, the diffusion thermopower can be expressed as<sup>14</sup>

$$S = \frac{k_B}{e\sigma} \int \sigma(E) \frac{(E - E_F)}{k_B T} \frac{\partial f}{\partial E} dE, \quad (1)$$

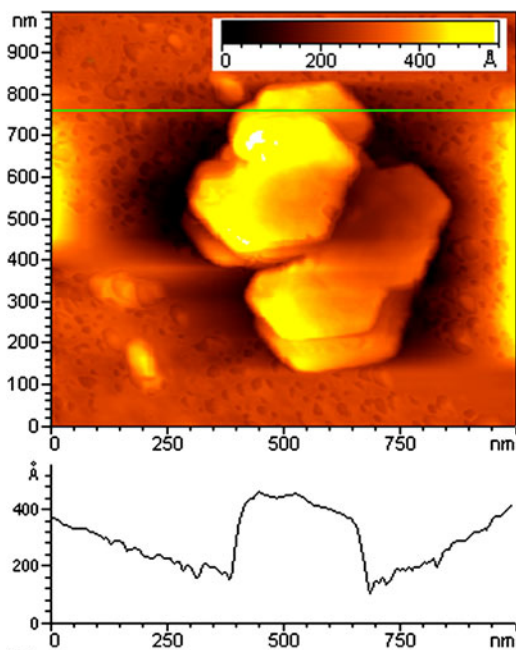
where  $f$ ,  $\sigma$ ,  $E_F$ , and  $k_B$  are the Fermi distribution function, electrical conductivity, Fermi energy, and Boltzmann constant, respectively. For a system with one type of carrier, the electrical conductivity  $\sigma$  in Eq. (1) is proportional to the product of carrier concentration and mobility and can be expressed as

$$\sigma = ne\mu, \quad (2)$$

where  $n$  and  $\mu$  are the carrier concentration and mobility, respectively. The mobility  $\mu$  of carriers can be expressed as  $\mu = e\tau/m^*$ , where  $\tau$  is the relaxation time associated with the carrier scattering process and  $m^*$  is their effective mass. Therefore, both the electrical resistivity and thermopower of a conductor depend on its carrier concentration and mean free path length between collisions. Figure 6 shows the carrier concentration and mobility for Bi<sub>0.5</sub>Sb<sub>1.5</sub>Te<sub>3</sub> sintered at different temperatures of 300–380 °C. Although the size of carrier concentration does not show a monotonic trend, the experimental data can be discussed in two categories in terms of sintering temperature. First, samples sintered between 300 and 360 °C do not show significant variation of the carrier concentration, having values in the range  $(0.9 \pm 0.2) \times 10^{19} \text{ cm}^{-3}$ . Second, the sample sintered at 380 °C shows different behavior as for resistivity and thermopower, exhibiting a very small Hall coefficient and so a dramatically increased carrier concentration of  $3.4 \times 10^{19} \text{ cm}^{-3}$ , being about 4.6 times of that for the



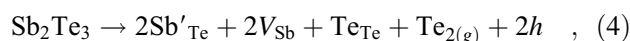
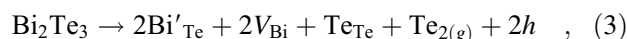
(a)



(b)

FIG. 3. (a) Scanning electron microscope (SEM) image of as-synthesized Bi<sub>0.5</sub>Sb<sub>1.5</sub>Te<sub>3</sub> showing the hexagonal nanoplatelets; (b) atomic force microscope image of as-synthesized Bi<sub>0.5</sub>Sb<sub>1.5</sub>Te<sub>3</sub> showing a thickness of about 30–50 nm. The profile shows only the lower platelet. There is another platelet on top of it.

sample sintered at 340 °C. The carrier mobility estimated from Eq. (2) shows a corresponding decrease for the 380 °C-sintered sample to account for its higher resistivity. Creation of p-type carriers in (Bi,Sb)<sub>2</sub>Te<sub>3</sub> is mainly attributed to the antistructure defects, which is generated by occupation of Te vacancy with Bi or Sb atoms.<sup>15,16</sup> Formation of antistructure defects can be described by the following equation:



where Bi'<sub>Te</sub> and Sb'<sub>Te</sub> are the antisite defects, V<sub>Bi</sub> and V<sub>Sb</sub> are the vacancies, and *h* is the electron hole. As the

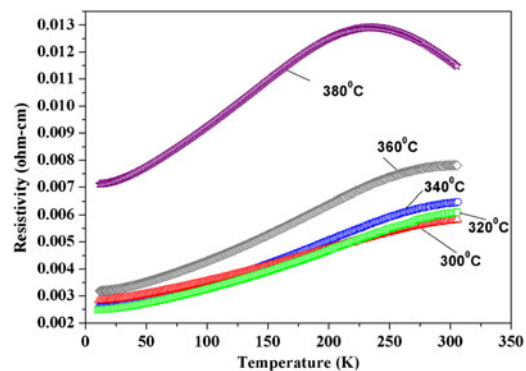


FIG. 4. Temperature dependence of electrical resistivity for Bi<sub>0.5</sub>Sb<sub>1.5</sub>Te<sub>3</sub> sintered at different temperatures of 300–380 °C in an evacuated ampoule.

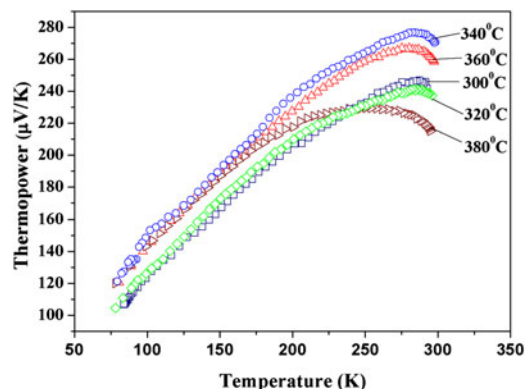


FIG. 5. Temperature dependence of thermopower for Bi<sub>0.5</sub>Sb<sub>1.5</sub>Te<sub>3</sub> sintered at different temperatures of 300–380 °C in an evacuated ampoule.

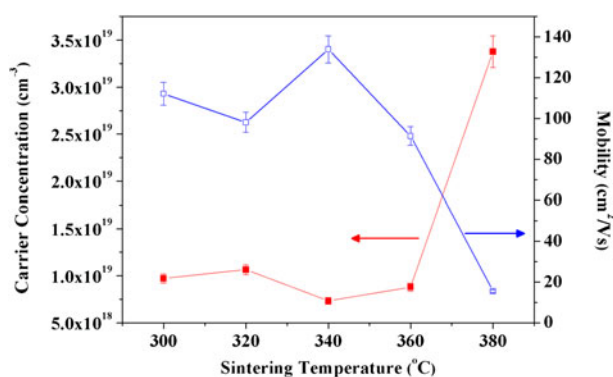


FIG. 6. Carrier concentration and mobility at room temperature for Bi<sub>0.5</sub>Sb<sub>1.5</sub>Te<sub>3</sub> sintered at different temperatures of 300–380 °C in an evacuated ampoule.

sintering temperature increases to 380 °C, a significant increase of hole concentration could be due to more antistructure defects generated in the sample, which is caused by slight evaporation of Te atoms.<sup>17</sup> Scattering from these defects as well as the fragmented structure of



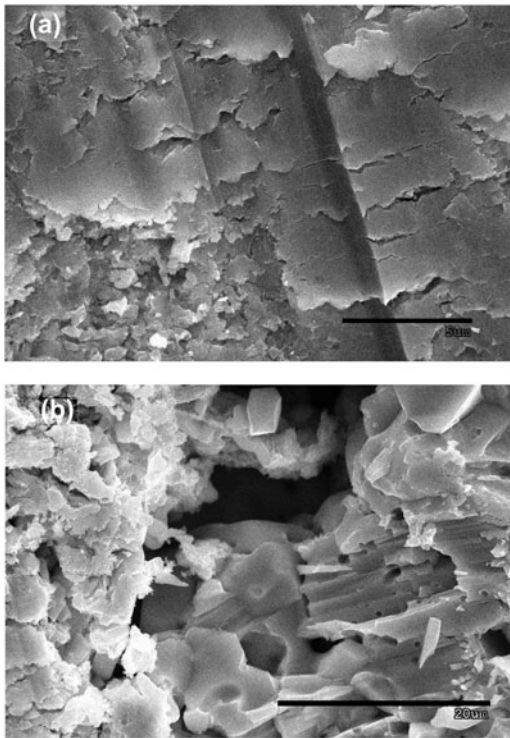


FIG. 7. The cross-sectional SEM micrographs of Bi<sub>0.5</sub>Sb<sub>1.5</sub>Te<sub>3</sub> sintered at (a) 340 °C and (b) 380 °C in an evacuated ampoule.

this sample [Fig. 7(b)] could cause the observed reduced mobility, as discussed below.

The thermopower of p-type (Bi,Sb)<sub>2</sub>Te<sub>3</sub> thermoelectric materials in the extrinsic conduction region can be expressed as<sup>17</sup>

$$S = \frac{k_B}{e} (\delta + C - \ln n) \quad , \quad (5)$$

where  $n$  is the hole concentration,  $\delta$  is associated with the scattering parameter, and  $C$  is a constant. According to the data shown in Figs. 5 and 6, it appears that the size of thermopower correlates well with the magnitude of the carrier concentration at room temperature. It can be readily seen that the sample having higher carrier concentration has a lower size of thermopower. According to Eq. (5), these results seem to suggest that all the samples follow a similar scattering mechanism or that the effect of the scattering parameter  $\delta$  on the thermopower is negligible. It is also interesting to note that the size of the mobility shows an opposite trend to that of the carrier concentration. In general, samples having higher resistivity are expected to show larger sizes of thermopower. However, the sample sintered at 380 °C shows the highest resistivity of 11.8 mΩ·cm at 295 K but the lowest thermopower of 215 μV/K at 295 K, whereas the sample sintered at 340 °C shows the resistivity of 6.4 mΩ·cm and relatively high thermopower of 273 μV/K at 295 K. These results seem to

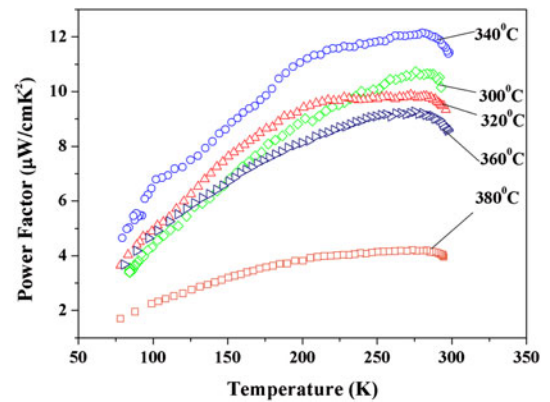


FIG. 8. Temperature dependence of the power factor  $\sigma S^2$  for Bi<sub>0.5</sub>Sb<sub>1.5</sub>Te<sub>3</sub> sintered at different temperatures of 300–380 °C in an evacuated ampoule.

contradict the general behavior. Even though the sample sintered at 380 °C has the highest carrier concentration of  $3.4 \times 10^{19} \text{ cm}^{-3}$ , its high resistivity can be ascribed to its low mobility of 15 cm<sup>2</sup>/V·s. In contrast, the sample sintered at 340 °C has the lowest carrier concentration of  $7.3 \times 10^{18} \text{ cm}^{-3}$ , but the highest mobility of 134 cm<sup>2</sup>/V·s among these samples. Figure 7 shows the cross-sectional SEM micrographs of Bi<sub>0.5</sub>Sb<sub>1.5</sub>Te<sub>3</sub> sintered at 340 °C and 380 °C, respectively. Figure 7(b) clearly shows the crevice of the sample sintered at 380 °C, which might hinder the carriers from transport across the sample and hence might be responsible for its small mobility. Moreover, morphologies for left, center and right areas in Fig. 7(b) are different from one another. This morphological heterogeneity might also be responsible for its low mobility and high resistivity.<sup>18</sup> Figure 8 shows the temperature dependence of the power factor for Bi<sub>0.5</sub>Sb<sub>1.5</sub>Te<sub>3</sub> samples sintered at different temperatures of 300–380 °C in an evacuated ampoule. The sample sintered at 340 °C shows the largest power factor of 11.6 μW/cm·K<sup>2</sup> at 295 K, whereas the sample sintered at 380 °C shows the smallest power factor of 3.9 μW/cm·K<sup>2</sup>. Since the sample sintered at 340 °C shows the largest power factor among these samples, the thermal conductivity measurement was only performed on this sample. Even though the power factor of 11.6 μW/cm·K<sup>2</sup> for the sample sintered at 340 °C is relatively small as compared to ~50 μW/cm·K<sup>2</sup> for the zone-melted counterpart, its thermal conductivity is rather small with the size of 0.37 W/m·K at 295 K as shown in Fig. 9.<sup>19–21</sup> Since the thermal conductivity of a material is determined by both the electronic and lattice contributions, i.e.,  $\kappa = \kappa_{el} + \kappa_{ph}$ , where  $\kappa_{el}$  and  $\kappa_{ph}$  represent the electronic and lattice thermal conductivity, respectively. The electronic contribution to thermal conductivity can be calculated using the Wiedemann–Franz law according to the relation between the electronic thermal conductivity  $\kappa_{el}$  and electrical conductivity  $\sigma$ , which can be expressed as<sup>22</sup>

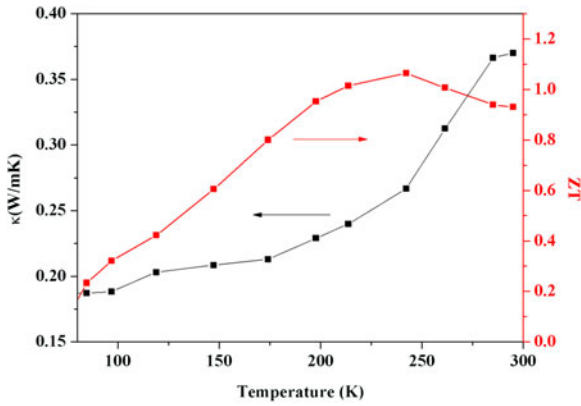


FIG. 9. Temperature dependence of the thermal conductivity and dimensionless figure of merit for Bi<sub>0.5</sub>Sb<sub>1.5</sub>Te<sub>3</sub> sintered at different temperatures of 300–380 °C in an evacuated ampoule. Since the vendor only provides the temperature coefficient of the resistivity (TCR) down to –80 °C for the sensor, we use TCR at room temperature as a constant in the whole investigated temperature range. The data below room temperature need further calibration for each sensor being used. However, the thermal conductivity obtained at 295 K is reliable.

$$\frac{\kappa_{el}}{\sigma} = \frac{\pi^2}{3} \left( \frac{k_B}{e} \right)^2 T = L_0 T \quad , \quad (6)$$

where  $L_0$  is the Lorenz number and has the size of  $2.45 \times 10^{-8} \text{ W}\cdot\Omega/\text{K}^2$ . According to Eq. (6), the calculated electronic thermal conductivity for the sample sintered at 340 °C is 0.11 W/m·K at 295 K and therefore the lattice thermal conductivity  $\kappa_{ph}$  would be 0.26 W/m·K at this temperature. The low electronic thermal conductivity is associated with its low electrical conductivity as compared to typical value of 1 mΩ·cm for Bi<sub>2-x</sub>Sb<sub>x</sub>Te<sub>3</sub> with good thermoelectric performance. The value of  $\kappa_{ph} = 0.26 \text{ W/m}\cdot\text{K}$  is quite small as compared to the samples fabricated using spark plasma sintering methods with the size of 0.5–0.8 W/m·K.<sup>19</sup> Holland<sup>23</sup> refined a model developed by Callaway<sup>24</sup> for expressing the lattice thermal conductivity:

$$\kappa_{ph} = \frac{1}{3} v_g \int_0^{\theta_D/T} c_V \tau d \left( \frac{\hbar\omega}{k_B T} \right) \quad , \quad (7)$$

where  $\theta_D$  is the Debye temperature,  $v_g$  is the velocity of phonons,  $\tau$  is the relaxation time, and  $\omega$  is the phonon angular frequency. An umklapp process, phonon–defect scattering, or phonon–grain boundary scattering would lead to reduction of  $\tau$ . Using Matthiessen’s rule,  $\tau$  can be expressed as

$$\frac{1}{\tau} = \frac{1}{\tau_u} + \frac{1}{\tau_{\text{defect}}} + \frac{1}{\tau_{\text{grain}}} \quad , \quad (8)$$

where  $\tau_u$ ,  $\tau_{\text{defect}}$ , and  $\tau_{\text{grain}}$  are the relaxation time due to the umklapp process, phonon–defect scattering, and

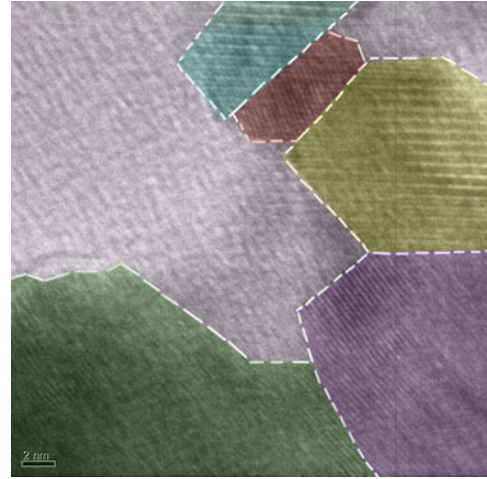


FIG. 10. Transmission electron microscope image showing the nano-sized grains for the sample sintered at 340 °C.

phonon–grain boundary scattering, respectively. The magnitude of  $\tau_{\text{grain}}$  is dependent of the average grains size, as described using the expression<sup>25</sup>:

$$\frac{1}{\tau_{\text{grain}}} = \frac{v_g}{d} \left( \frac{1 - p(\omega)}{1 + p(\omega)} \right) \quad , \quad (9)$$

where  $p(\omega)$  is the probability of specular reflection and  $d$  is the average grain size. Suppose that the phonon spectrum is not drastically altered, the significant reduction of thermal conductivity should be attributed to a strong scattering of phonons.<sup>26</sup> Figure 10 shows the TEM image of the sample sintered at 340 °C. The image clearly shows nanosized grains in the microstructure of the sample. According to Eq. (9), a small average size of these nanosized grains is expected to have a small size of  $\tau_{\text{grain}}$ , which in turn one could expect a small  $\kappa_{ph}$  according to Eqs. (7) and (8). Besides, since the density of compacted and sintered sample is less than 90% of its theoretical density, the porous microstructure is expected. Porosity would lead to further reduction of thermal conductivity<sup>27</sup>. Therefore, the small observed  $\kappa_{ph}$  could be mainly attributed to the nanosized grains and porosity of the sample. The dimensionless thermoelectric figure of merit  $ZT$  is calculated to be 0.93 at 295 K shown in Fig. 8 for the sample sintered at 340 °C.

#### IV. CONCLUSIONS

In summary, the hydrothermally synthesized nanoplatelets of Bi<sub>0.5</sub>Sb<sub>1.5</sub>Te<sub>3</sub> are compacted and sintered in an evacuated ampoule at various temperatures of 300–380 °C for optimizing the thermoelectric characteristics. The sample sintered at 340 °C shows the largest dimensionless figure of merit  $ZT = 0.93$  at 295 K among the samples. It has very low thermal conductivity of

0.37 W/m·K as compared to the (Bi,Sb)<sub>2</sub>Te<sub>3</sub> alloys fabricated using other methods.

## ACKNOWLEDGMENT

This work is supported by the National Science Council of Taiwan, Republic of China, Grant Nos. NSC 95-2112-M-018-006-MY3 and NSC 98-2112-M-018-005-MY3.

## REFERENCES

1. L.D. Hicks and M.S. Dresselhaus: Effect of quantum-well structures on the thermoelectric figure of merit. *Phys. Rev. B* **47**, 12727 (1993).
2. L.D. Hicks and M.S. Dresselhaus: Thermoelectric figure of merit of a one-dimensional conductor. *Physica B* **47**, 6631 (1993).
3. B. Poudel, Q. Hao, Y.L. Ma, Y.C. Lan, A. Minnich, B. Yu, X. Yan, D.Z. Wang, A. Muto, D. Vashaee, X.Y. Chen, J.M. Liu, M.S. Dresselhaus, G. Chen, and Z. Ren: High-thermoelectric performance of nanostructured bismuth antimony telluride bulk alloys. *Science* **320**, 63 (2008).
4. W. Xie, X. Tang, Y. Yan, Q. Zhang, and T.M. Tritt: Unique nanostructures and enhanced thermoelectric performance of melt-spun BiSbTe alloys. *Appl. Phys. Lett.* **94**, 102111 (2009).
5. X.B. Zhao, X.H. Ji, Y.H. Zhang, T.J. Zhu, J.P. Tu, and X.B. Zhang: Bismuth telluride nanotubes and the effects on the thermoelectric properties of nanotube-containing nanocomposites. *Appl. Phys. Lett.* **86**, 062111 (2005).
6. W. Lu, Y. Ding, Y. Chen, Z.L. Wang, and J. Fang: Bismuth telluride hexagonal nanoplatelets and their two-step epitaxial growth. *J. Am. Chem. Soc.* **127**, 10112 (2005).
7. Y. Deng, C.W. Cui, N.-L. Zhang, T.H. Ji, Q. Yang, and L.L. Guo: Fabrication of bismuth telluride nanotubes via a simple solvothermal process. *Solid State Commun.* **138**, 111 (2006).
8. C.-J. Liu, G.-J. Liu, C.-W. Tsao, Y.-F. Lu, and L.-S. Chang: Improvement of thermoelectric power factor of hydrothermally prepared Bi<sub>0.5</sub>Sb<sub>1.5</sub>Te<sub>3</sub> compared with its solvothermally prepared counterpart. *J. Electron. Mater.* **38**, 1499 (2009).
9. W. Lu, Y. Ding, Y. Chen, Z.L. Wang, and J. Fang: Bismuth telluride hexagonal nanoplatelets and their two-step epitaxial growth. *J. Am. Chem. Soc.* **127**, 10112 (2005).
10. C.-J. Liu, G.-J. Liu, C.-W. Tsao, Y.-F. Lu, and L.-S. Chang: Thermoelectric characteristics of solvothermally prepared (Bi,Sb)<sub>2</sub>Te<sub>3</sub> mats containing nanosize of sheet-tubes, in *Proceedings of 26th International Conference on Thermoelectrics*, June 3–5, 2007, p. 30.
11. J.M. Schultz, J.P. McHugh, and W.A. Tiller: Effects of heavy deformation and annealing on the electrical properties of Bi<sub>2</sub>Te<sub>3</sub>. *J. Appl. Phys.* **33**, 2443 (1962).
12. D. Zhao, B.-P. Zhang, W.S. Liu, H.L. Zhang, and J.-F. Li: Effects of annealing on electrical properties of n-type Bi<sub>2</sub>Te<sub>3</sub> fabricated by mechanical alloying and spark plasma sintering. *J. Alloy. Comp.* **467**, 91 (2009).
13. S.E. Gustafsson: Transient plane source techniques for thermal conductivity and thermal diffusivity measurements of solid materials. *Rev. Sci. Instrum.* **62**, 797 (1991).
14. N.F. Mott and E.A. Davis: *Electronic Process in Non-crystalline Materials*, 2nd ed. (Clarendon, Oxford, 1979), p. 52.
15. Z. Starý, J. Horák, M. Stordeur, and M. Stölzer: Antisite defects in Sb<sub>2–x</sub>Bi<sub>x</sub>Te<sub>3</sub> mixed crystals. *J. Phys. Chem. Solids* **49**, 29 (1988).
16. X.A. Fan, J.Y. Yang, W. Zhu, S.Q. Bao, X.K. Duan, C.J. Xiao, Q.Q. Zhang, and Z. Xie: Effect of nominal Sb<sub>2</sub>Te<sub>3</sub> content on thermoelectric properties of p-type (Bi<sub>2</sub>Te<sub>3</sub>)<sub>x</sub>(Sb<sub>2</sub>Te<sub>3</sub>)<sub>1–x</sub> alloy by MA-HP. *J. Phys. D: Appl. Phys.* **39**, 5069 (2006).
17. D.B. Hyun, T.S. Oh, J.S. Hwang, and J.D. Shim: Effect of excess Te addition on the thermoelectric properties of the 20% Bi<sub>2</sub>Te<sub>3</sub>-80% Sb<sub>2</sub>Te<sub>3</sub> single crystal and hot-pressed alloy. *Scr. Mater.* **44**, 455 (2001).
18. C.-J. Liu, T.-W. Wu, L.-S. Hsu, C.-J. Su, C.-C. Wang, and F.-S. Shieu: Transport properties of spiral carbon nanofiber mats containing Pd metal clusters using Pd<sub>2</sub>(dba)<sub>3</sub> as catalyst. *Carbon* **42**, 2635 (2004).
19. J. Jiang, L.D. Chen, S.Q. Bai, Q. Yao, and Q. Wang: Thermoelectric properties of textured p-type (Bi,Sb)<sub>2</sub>Te<sub>3</sub> fabricated by spark plasma sintering. *Scr. Mater.* **52**, 347 (2005).
20. J.L. Cui, H.F. Xu, and W.J. Liu: Preparation and thermoelectric properties of p-type (Ga<sub>2</sub>Te<sub>3</sub>)<sub>x</sub>-(Bi<sub>0.5</sub>Sb<sub>1.5</sub>Te<sub>3</sub>)<sub>1–x</sub> ( $x = 0–0.2$ ) alloys prepared by spark plasma sintering. *Intermetallics* **15**, 1466 (2007).
21. J. Yang, T. Aizawa, A. Yamamoto, and T. Ohta: Effect of processing parameters on thermoelectric properties of p-type (Bi<sub>2</sub>Te<sub>3</sub>)<sub>0.25</sub>(Sb<sub>2</sub>Te<sub>3</sub>)<sub>0.75</sub> prepared via BMA-HP method. *Mater. Chem. Phys.* **70**, 90 (2001).
22. C. Kittel: *Introduction to Solid State Physics*, 6th ed. (John Wiley & Sons, New York), p. 152.
23. M.G. Holland: Analysis of lattice thermal conductivity. *Phys. Rev.* **132**, 2461 (1963).
24. J. Callaway: Model for lattice thermal conductivity at low temperatures. *Phys. Rev.* **113**, 1046 (1959).
25. J.E. Graebner, M.E. Reiss, and L. Seibles: Phonon scattering in chemical-vapor-deposited diamond. *Phys. Rev. B* **50**, 3702 (1994).
26. W.J. Xie, J. He, H.J. Kang, X.F. Tang, S. Zhu, M. Laver, S.Y. Wang, J.R.D. Copley, C.M. Brown, Q.J. Zhang, and T.M. Tritt: Identifying the specific nanostructures responsible for the high thermoelectric performance of (Bi,Sb)<sub>2</sub>Te<sub>3</sub> nanocomposites. *Nano Lett.* **10**, 3283 (2010).
27. P.E. Hopkins, P.T. Rakich, R.H. Olsson, I.F. El-kady, and L.M. Phinney: Origin of reduction in phonon thermal conductivity of microporous solids. *Appl. Phys. Lett.* **95**, 161902 (2009).